Cross-β Spine Architecture of Fibrils Formed by the Amyloidogenic Segment NFGSVQFV of Medin from Solid-State NMR and X-ray Fiber Diffraction Measurements[†]

Jillian Madine,[‡] Alastair Copland,[§] Louise C. Serpell,[§] and David A. Middleton*[,‡]

School of Biological Sciences, University of Liverpool, Crown Street, Liverpool L69 7ZB, United Kingdom, and Department of Biochemistry, School of Life Sciences, University of Sussex, Falmer, Brighton BN1 9QG, United Kingdom

Received November 24, 2008; Revised Manuscript Received February 4, 2009

ABSTRACT: Over 30 polypeptides are known to assemble into highly ordered fibrils associated with pathological disorders known collectively as amyloidoses. Structural studies of short model peptides are beginning to reveal trends in the types of molecular interactions that drive aggregation and stabilize the packing of β-sheet layers within fibrillar assemblies. This work investigates the molecular architecture of fibrils formed by the peptide $AMed_{42-49}$ representing residues 42−49 of the 50 amino acid polypeptide medin associated with aortic medial amyloid, the most common form of senile localized amyloid. The peptide aggregates within 2 days to form bundles of microcrystalline-like needles displaying a high degree of order. Fibrils were prepared from peptides containing up to 23 ^{13}C labels, and the solid-state nuclear magnetic resonance (SSNMR) method rotational resonance (RR) was used to determine constraints on the distances between selective atomic sites within fibrils. The constraints are consistent with unbroken β-strands hydrogen bonded in a parallel in-register arrangement within β-sheets. Further RR measurements identify close (>6.5 Å) contacts between residues F43 and V46 and between S45 and V46, which can only occur between β-sheet layers and which are consistent with two principal models of β-sheet arrangements. X-ray fiber diffraction from partially aligned fibrils revealed the classical amyloid diffraction pattern, and comparison of patterns calculated from model coordinates with experimental data allowed determination of a consistent molecular model.

All normally soluble proteins and peptides have the latent ability to misfold and aggregate to form insoluble, highly ordered amyloid or amyloid-like fibril assemblies. Some 30 polypeptides are known to undergo aggregation in vivo, and many of these are associated with extracellular deposits or intracellular inclusions that are the pathological hallmark of misfolding disorders known collectively as amyloidoses (*1*). The prevalence of amyloid diseases in the aging population is a major public health issue for Western countries, and there are clear socioeconomic incentives for targeting protein aggregates with therapeutic intervention (*2*).

Amyloid fibrils exhibit a common molecular architecture in which arrays of β-strands are connected by hydrogen bonds oriented parallel to the fiber long axis, into an array known as a cross-β structure. The substructure of mature fibrils consists of one or more protofilament units, which can assemble laterally or intertwine in various ways as rope-like or ribbon-like modifications to the common fibrillar framework (*3*). Advances in crystallography and solid-state nuclear magnetic resonance (SSNMR[1]) are helping to elucidate the critical structural elements of diverse protein sequences, beyond the cross-β motif, that stabilize the fibrillar end-products of aggregation. X-ray analysis of microcrystals of short amyloidogenic peptide segments have indicated that protofilaments consist of a common cross-β spine formed by a minimum of two β-sheet layers (*4*), which can pack together with interdigitated side groups, forming a steric zipper (*5*). An alternative main-chain interface between opposing sheets has recently been reported for the segment NNFGAIL from the pancreatic islet amyloid polypeptide amylin (*6*). The related amylin peptide segments SNNFGAILSS, NFGAIL, and FGAIL all aggregate into different fibrillar assemblies, however, thus highlighting how substantial morphological variations can originate from subtle modifications to protein sequence (*7*). Structural constraints from SSNMR measurements have enabled detailed models to be proposed for several amyloid assemblies, both for intact native polypeptides and for segments thereof (*8*). These include the amyloid β-peptide (*9, 10*), amylin (*11*), β_2-microglobulin (*12*), transthyretin (*13*), a prion segment (*14*), and α-synuclein (*15*). A common motif emerging from the

* To whom correspondence should be addressed. E-mail: middleda@liv.ac.uk. Tel: +44 151 7954457. Fax: +44 151 795 4406.

[†] Funding information: the Alzheimer's Research Trust supports a fellowship to J.M. L.C.S. is supported by funding from the BBSRC and Alzheimer's Research Trust, and D.A.M. is supported by funding from the BBSRC and the British Heart Foundation.

[‡] University of Liverpool.

[§] University of Sussex.

[1] Abbreviations: SSNMR, solid-state nuclear magnetic resonance; DLS, dynamic light scattering; CP-MAS, cross-polarization magic-angle spinning; $AMed_{42-49}$, a peptide comprising residues 42−49 of medin; AMA, aortic medial amyloid; RR, rotational resonance; DARR, dipolar assisted rotational resonance; DQ-HLF NMR, double-quantum heteronuclear local field NMR.

10.1021/bi802164e CCC: $40.75
Published on Web 03/23/2009

Table 1: Summary of the Nomenclature for the ^{13}C-Labeled Peptides Used in This Work and the Figures in Which They Appear[a]

name	labeling pattern	experiments
[C′-^{13}C-F43]AMed$_{42-49}$	N<u>F(C′)</u>GSVQFV	Figures 1, 4
[U-^{13}C-NFGSV]AMed$_{42-49}$	<u>NFGSV</u>QFV	Figures 3, 5, 6
[U-^{13}C-QFV]AMed$_{42-49}$	NFGSV<u>QFV</u>	Figure 3
[Cα-^{13}C-F43]AMed$_{42-49}$	N<u>F(Cα)</u>GSVQFV	Figure 4

[a] Labeled residues are underlined. "U" denotes uniformly labeled and C′ denotes the carbonyl carbon. All peptides were N-acetylated and C-terminally amidated.

limited structural information for longer polypeptides is a repeating structure within protofilaments consisting of two or more β-sheet layers punctuated by turns or regions of disorder (*9*−*12, 15*).

Aortic medial amyloid (AMA) is found in 97% of individuals over the age of 50 and is the most common form of localized amyloid (*16*). The main constituent of AMA is a 50 amino acid polypeptide derived from the proteolysis of lactadherin, a mammary epithelial cell expressed glycoprotein that is secreted as part of the milk fat globule membrane (*17*). The impact of AMA on cardiovascular health is unknown, but there is speculation that the amyloid deposits contribute to age-related diminished elasticity of the vessels and also experimental evidence that soluble oligomeric intermediates may underlie the pathogenesis of a sporadic thoracic aortic aneurysm (*18*). The 18−19 C-terminal residues of medin constitute the amyloid-promoting region (*19*), and an octapeptide segment within this region, NH_2-NFGSVQFV-COOH (AMed$_{42-49}$), alone forms typical well-ordered amyloid fibrils (*17*). The smaller truncated fragment NFGSVQ also forms typical amyloid fibrils, whereas the shorter pentapeptide fragment, NFGSV, forms a gel. Substitution of the phenylalanine residue in these peptides with either alanine or isoleucine significantly reduced their amyloidogenic potential (*20*), supporting a general hypothesis that aromatic $\pi-\pi$ interactions can play a role in stabilizing fibril assemblies (*21*).

Here structural constraints measured using SSNMR have been exploited to determine the molecular arrangement within the cross-β spine of AMed$_{42-49}$ fibrils. Rotational resonance (RR) SSNMR measurements of interatomic distance limits were performed on peptides labeled with ^{13}C either at a selective pair of sites or at multiple sites across a block of five amino acids. The measured distances place strong constraints on the alignment of hydrogen bonded β-strands and on the stacking geometry of β-sheet layers. With additional analysis of X-ray fiber diffraction data, a plausible model is proposed for the molecular architecture of the cross-β spine. The results are discussed in the context of sequence requirements for stabilization of amyloid assemblies in general.

EXPERIMENTAL SECTION

Preparation of Fibrils. Synthetic AMed$_{42-49}$ was purchased from Peptide Protein Research (U.K.) Ltd. The various labeling patterns for the peptides are summarized in Table 1. Fibrils of AMed$_{42-49}$ were prepared essentially as described by Westermark et al. (*17*). Briefly, the peptides were subjected to three dissolution−evaporation cycles with hexafluoroisopropanol to break up any initial aggregates. The peptides were dissolved in dimethylsulfoxide (DMSO) and added to double distilled H_2O to a final DMSO concentration of 10% (v/v) and a peptide concentration of 1 mg/mL. The peptide is not soluble below 10% DMSO. The solution was incubated with agitation at room temperature for 4 d, and fibrils were harvested by spinning down in a benchtop centrifuge for 30 min.

Analysis of Fibril Growth and Morphology. Aggregation was monitored using dynamic light scattering (DLS). A series of 20 measurements of 10 s each were taken at 30 °C on a Zetasizer Nano DLS machine from Malvern Instruments, and averaged profiles were produced. Particle size distributions are expressed as a percentage of the total volume of the solution that scatters light (% volume), derived from intensity of scattered light measured after taking into account the mass/weight distribution. It is therefore a weighted value to reduce the effects of single large particles from dominating the profiles and masking smaller particles. Morphologies of the insoluble aggregates were analyzed by transmission electron microscopy using negative staining (4% uranyl acetate). Peptide suspensions (10 μL) were loaded onto carbon-coated copper grids and visualized on a Tecnai 10 electron microscope at 100 kV.

Solid-State NMR Experiments. All NMR experiments were performed on hydrated fibrils (5 mg of peptide unless stated otherwise) using a Bruker Avance 400 spectrometer operating at a magnetic field of 9.3 T. Experiments were carried out with cross-polarization magic-angle spinning (CP-MAS) at −10 °C to reduce interference from molecular dynamics. Samples were packed into a 4 mm zirconium rotor and rotated at the magic angle at rates between 4 kHz and 13 kHz, while maintaining the spinning rate automatically to within ±1 Hz. All experiments utilized an initial 4.0 μs ^{1}H 90° excitation pulse length, a 1 ms Hartmann−Hahn contact time at a matched ^{1}H field of 65 kHz, a two-pulse phase modulation proton decoupling (*22*) at a field of 85 kHz during signal acquisition, and a 2 s recycle delay.

Dipolar assisted rotational resonance (DARR) spectra (*23*) were recorded with 128 hypercomplex points in the indirect dimension (t_1), with a mixing time of 20 ms during which the proton field was adjusted to the spinning frequency of 8 kHz. One-dimensional RR experiments were carried out by adjusting the sample spinning rate (ω_R) to the difference between the resonance frequencies ($\Delta\Omega_{CC}$) (i.e., the $n = 1$ RR condition) for the pairs of spins selected. After cross-polarization, ^{13}C longitudinal difference polarization was created with a nonselective 4 μs $\pi/2$ pulse followed by a train of 18 delays alternating with nutations for tailored excitation pulses, representing an overall π pulse of 30 μs, to invert the ^{13}C spin polarization for one of the spins selectively. After a mixing period, the ^{13}C magnetization was returned to the transverse plane by a second nonselective $\pi/2$ pulse before digitization of the free-induction decay. A series of experiments using mixing periods of up to 40 ms were performed to measure the time dependence of difference polarization. Curves representing exchange of Zeeman order were obtained from the difference in intensities for the selected pair of peaks. Peak intensities were adjusted so as to take into account the population of labeled peptides in excess that did not contribute to the RR effect. Two-dimensional exchange spectra were obtained with the same conditions as for the DARR spectra, except for the spinning rate, which was adjusted to the RR condition for a given

pair of spins, and for the proton decoupling field (100 kHz) applied during a mixing time of 30 ms. Double-quantum heteronuclear local field (DQ-HLF) experiments at a spinning rate of 6 kHz were carried out essentially as described by Feng et al. (*24*) but adapted as a two-dimensional experiment with 32 t_1 points in the indirect dimension. Double quantum coherences were excited using C7 (*25*) and evolved over two rotor cycles ($2 \times t_R$), during which proton−proton dipolar interactions were removed by frequency-switched Lee−Goldberg decoupling (*26*) for a period *t*. During this period two 180° pulses were applied at the ^{13}C frequency, one after t_R and one after $2t_R$ to refocus the DQ frequencies. Signal amplitudes *a* were measured as a function of *t* over a series of experiments in which *t* was incremented from 0 to t_R.

Numerical Simulations of Magnetization Exchange Curves. Simulation of magnetization exchange between the C′ and the Cα spins of F43 at $n = 1$ RR were carried out with a Fortran computer program written specifically for that purpose. Curves were calculated as described elsewhere (*27*) and were a function of the distance-dependent $^{13}C-^{13}C$ dipolar coupling constant d_{CC} corresponding to specific β-strand alignments and to a range of values for the zero quantum relaxation time T_2^{ZQ}. The T_2^{ZQ} values used in these simulations were taken from the inverse sum of the off-RR line widths plus or minus 1.5 ms. Values for ^{13}C chemical shift anisotropy and asymmetry parameters were measured from solid phenylalanine.

X-ray Diffraction. A droplet of solution of seeded amyloid fibrils of $AMed_{42-49}$ was placed between two wax-filled capillary tubes on a stretch frame, and the fibrils were allowed to dry to form a partially aligned fiber sample as previously described (*28*). X-ray diffraction data were collected using a Rigaku rotating anode (Cu Kα) and RAxis 4++ detector with the specimen to a detector distance of 160 mm and exposure times of 10−20 min. X-ray diffraction patterns were examined using a computer program called CLEARER (*29*). Positions of diffraction signals were measured and potential unit cell dimensions were explored using the unit cell determination algorithm within CLEARER. Constraints from SSNMR experiments were also taken into account, and possible unit cell dimensions were determined. The optimum unit cell was selected that was also consistent with other data.

Calculation of Diffraction Patterns. Fiber diffraction patterns were generated from a range of model coordinates contained within an orthogonal unit cell containing two pairs of β-strands in different arrangements with dimensions 29.2 Å, 36.6 Å, 9.52 Å. The original structural models originating from SSNMR were duplicated in the cell direction to fill the determined unit cell, resulting in four β-sheets with each sheet containing two hydrogen bonded β-strands. The geometry of a fiber was taken into account, and the fiber axis was defined as parallel to the hydrogen bonding direction (*28, 29*). Calculated diffraction patterns were compared with the experimental diffraction pattern by overlaying the two patterns and examining close matches between the experimental and the calculated diffraction signal positions.

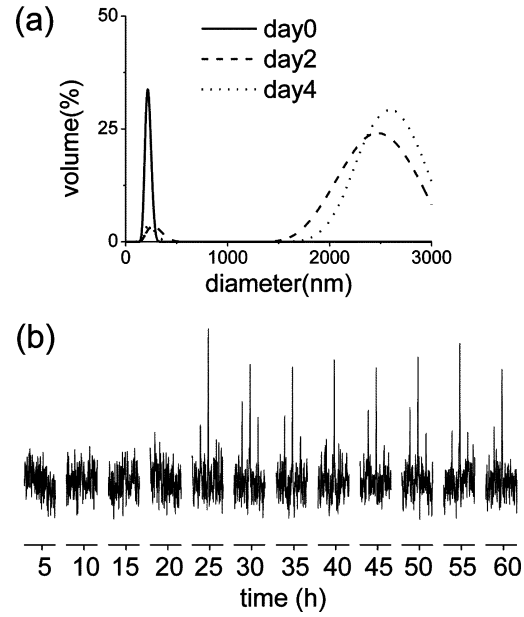

FIGURE 1: Experiments to monitor the rate of aggregation of $AMed_{42-49}$. (a) DLS profiles of particle size in an aqueous solution of 1 mg/mL of $AMed_{42-49}$ immediately after preparation (solid line) and after incubation at 25 °C for 2 d (dashed line) and 4 d (dotted line). (b) A series of ^{13}C CP-MAS spectra obtained at 5 h intervals from an initial solution of 1 mg [C′-^{13}C-F43]$AMed_{42-49}$ in 100 μL aqueous buffer. The sample spinning rate was 4 kHz, and the temperature was 25 °C. Each spectrum is the result of accumulating 18 000 scans. At the later time points (>20 h), each central line is flanked by two visible spinning side bands.

RESULTS

Fibril Growth and Morphology. Aggregation of $AMed_{42-29}$ was followed using DLS to monitor the particle sizes formed by the peptide initially and after 2 days and 4 days of incubation at 25 °C. Despite pretreatment of $AMed_{42-29}$ with hexafluoroisopropanol and DMSO, the peptide (1 mg/mL) formed aggregates approximately 200 nm in diameter immediately after dissolution, although no visible evidence of insoluble material was found at this early stage (Figure 1a, solid line). After incubation for 2 days and longer, the amount of 200 nm species had decreased and was replaced by a larger dominant species of around 2400−2600 nm in diameter (Figure 1a, dashed and dotted lines). The solution had become visibly cloudy by this stage, and insoluble aggregates could be isolated by centrifugation.

The feasibility of using ^{13}C CP-MAS NMR to monitor aggregation of amyloidogenic peptides in situ was investigated in the course of this work. A 100 μL aqueous solution containing 1 mg of [C′-^{13}C-F43]$AMed_{42-49}$ was rotated at the magic angle at a rate of 4 kHz, and aggregation was monitored in real time. Signals from monomeric peptide or small soluble oligomers are not observed in the CP-MAS spectrum because rapid isotropic molecular reorientation averages to zero the $^1H-^{13}C$ dipolar interactions that are necessary for cross-polarization at the short contact time of 1 ms. When larger aggregates and insoluble precipitates are formed, the reduced molecular dynamics allow cross-polarization to occur, and signals can in principle be detected by accumulating sufficient numbers of transients. Here each spectrum was collected over 5 h, covering a total period of 70 h (Figure 1b). No signals consistent with large aggregates were detected over the first 20 h, but subsequent spectra

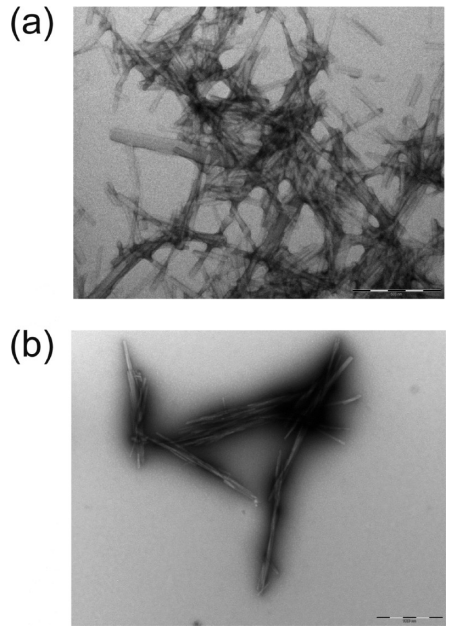

FIGURE 2: Negative stain electron micrographs of $AMed_{42-49}$ aggregates (harvested after incubation of 1 mg/mL peptide in aqueous solution for 24 h) at two magnifications. (a) Scale bar = 500 nm. (b) Scale bar = 1000 nm.

showed distinct peaks consistent with large soluble or insoluble species. After 20 h the overall signal intensity remained relatively constant within the level of the noise, suggesting that aggregation had reached the end-point by 25 h under the conditions of this experiment. Sample dehydration, which can occur during long CP-MAS experiments, could give rise to deposition of solid, nonfibrillar peptides on the wall of the sample rotor, which may be misinterpreted as fibril precipitation. Qualitative examination of the sample at the end of the experiment indicated that the peptide had formed a precipitate but remained hydrated and could be removed from the sample rotor by pipetting. These results thus demonstrate that SSNMR can detect aggregation in real time, although all further analysis below was performed on aggregates formed under conventional conditions at the lower initial peptide concentration of 1 mg/mL.

Analysis of the aggregate ultrastructure by electron microscopy (Figure 2) revealed bundles of rather wide unbranched filaments approximately 10−20 nm in diameter, similar to the needle-like microcrystalline clusters formed by other short peptide fragments (*4, 5*). The micrographs suggest that the fibrils have a high degree of order, which is favorable for analysis by SSNMR and X-ray fiber diffraction. Analysis of the material removed from the rotor after the experiment shown in Figure 1b confirmed that fibrils were present in the precipitate (data not presented).

Structural Analysis by SSNMR. Protein and peptide secondary structures can be estimated from isotropic ^{13}C chemical shift values to predict backbone torsional angles. Here two-dimensional $^{13}C-^{13}C$ DARR spectra were obtained from ^{13}C-labeled $AMed_{42-49}$ fibrils to facilitate residue-specific peak assignments and to measure chemical shifts. Spectra were acquired for two fibril samples: in one sample the five N-terminal residues were uniformly labeled (i.e., [U-^{13}C-NFGSV]$AMed_{42-49}$), and in the other the 3 C-terminal residues were labeled (i.e., [U-^{13}C-QFV]$AMed_{42-49}$). This division of labeling was done to assist assignment by

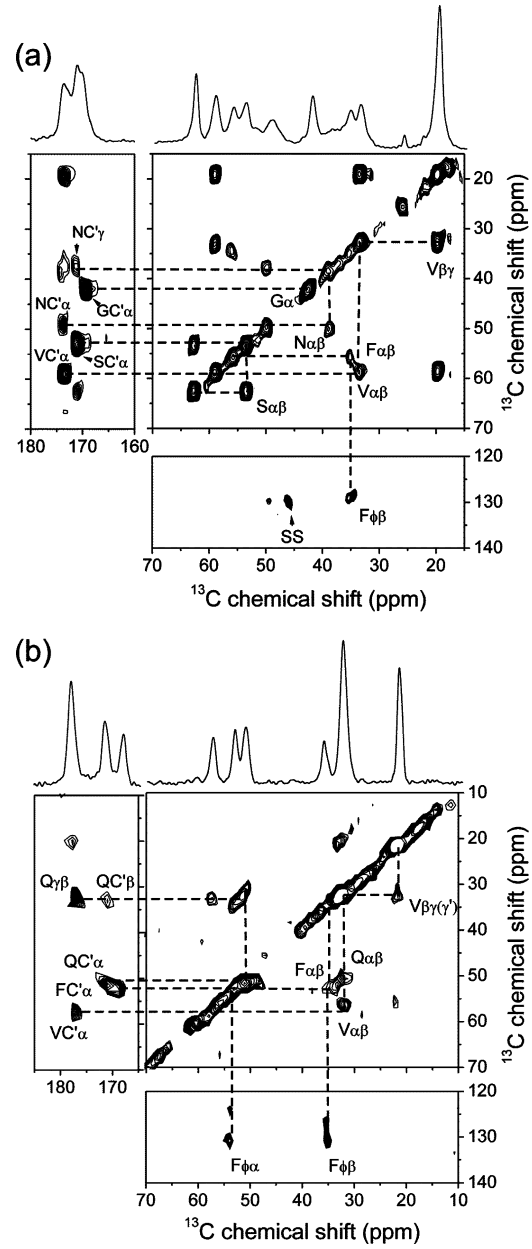

FIGURE 3: Two-dimensional ^{13}C DARR SSNMR spectra of block $^{13}C/^{15}N$-labeled $AMed_{42-49}$ with assignments. (a) Spectrum of [U-^{13}C,^{15}N-NFGSV]$AMed_{42-49}$. (b) Spectrum of [U-^{13}C,^{15}N-QFV]$AMed_{42-49}$. Above the DARR spectra are shown the one-dimensional CP-MAS spectra of the same samples (acquired at a MAS rate of 8 KHz).

reducing crowding and overlap in the spectra, particularly in the case of the two valine and two phenylalanine residues. The spectra and peak assignments are shown in Figure 3, and the chemical shifts are summarized in Table 2. Backbone ϕ and Ψ angles predicted using the computer program TALOS (*30*), summarized in Table 3, are consistent with the fibrillar peptide, adopting an unbroken β-strand.

Fibrils usually contain one or more protofilament units, and each protofilament may consist of layers of β-sheets running parallel with the fibril long axis. Hydrogen bonds between neighboring peptide β-strands within each β-sheet layer are aligned parallel or antiparallel to each other and may be in-register or out-of-register (staggered) such that the terminal ends are exposed. Distance constraints on strand alignments within β-sheets can be obtained with ^{13}C RR

Table 2: Summary of ^{13}C Chemical Shift Values for the Carbonyl (C′), Cα, and Side Chain Positions of $AMed_{42-49}$ Fibrils[a]

residue	chemical shift (ppm)				
	C′	Cα	Cβ	Cγ(γ′)[b]	Cϕ[c]
N42	173.6	50.0	38.7	171.2	
F43	170.4	55.8	35.1	136.9	128.5
G44	169.5	42.7			
S45	171.0	53.6	62.7		
V46	173.4	58.8	33.6	18.3	
Q47	171.3	51.1	32.9	176.6	
F48	167.6	53.5	32.0	137.7	130.0
V49	176.9	57.4	32.8	21.9	

[a] Values (referenced to external adamantane at 37.8 ppm) were measured from ^{13}C spectra of [C′-^{13}C-F43]$AMed_{40-49}$, [U-^{13}C-NFGSV]$AMed_{40-49}$, and [U-^{13}C-QFV]$AMed_{40-49}$. [b] Chemical shifts for Cγ and Cγ′ are equivalent for V2 and V8. [c] Chemical shifts denote the midpoint of the range.

Table 3: Summary of Backbone Torsional Angles for $AMed_{42-49}$ Fibrils Predicted from ^{13}C and ^{15}N Chemical Shifts Using TALOS (*30*)

residue	torsional angle	
	ϕ	Ψ
N42		
F43	−98 ± 11	114 ± 11
G44	−119 ± 18	134 ± 19
S45	−125 ± 21	134 ± 26
V46	−128 ± 18	140 ± 15
Q47	−120 ± 11	132 ± 12
F48	−128 ± 30	133 ± 31
V49		

NMR measurements of fibrils containing mixtures of peptides labeled either at the Cα or C′ positions of specific amino acid residues (*31*−*33*). Sites are chosen so that for some possible alignments, but not others, the intermolecular Cα−C′ distance for hydrogen bonded strands is less than 6 Å, which is generally the upper limit of detection by RR. Here the peptide alignment RR measurements were performed on fibrils prepared from a mixture of [α-^{13}C-F43]$AMed_{42-49}$ and [C′-^{13}C-F43]$AMed_{42-49}$ in a 5:1 molar ratio. This ratio ensures that each C′-labeled peptide has a probability of being hydrogen bonded to at least one α-^{13}C-labeled peptide, although in practice the exact ratio is not critical when the signal-to-noise ratio is high. Spectra were obtained at the first order ($n = 1$) RR condition of 11 473 Hz after creating an initial condition of difference polarization, followed by a variable mixing period. A clear attenuation of the difference intensity is observed after a mixing period of 30 ms, which signifies that the Cα−C′ intermolecular distance is close enough to permit the exchange of Zeeman order mediated by dipolar interactions (Figure 4a). The spectra are thus consistent with a Cα−C′ distance (6 Å or less) that is diagnostic of parallel strands that are in-register or out-of-register by one residue (Figure 4b). For in-register antiparallel strands, the distance exceeds 16 Å, and so this arrangement can therefore be excluded.

An attempt was made to improve the precision of the Cα−C′ distance constraint by analyzing the time dependence of Zeeman exchange as measured from the difference intensities (Figure 4c). The plots are compared with numerically simulated curves corresponding to the distances for in-register and ±1 out-of-register strands. A distance of 4.9 Å (in-register) corresponds to a dipolar coupling constant d_{CC} of 63 Hz, and a distance of 5.8 Å (±1 out-of-register) corresponds to 37 Hz. Several curves were calculated for the d_{CC} values for each geometry, spanning a range that is dictated by uncertainties in the value of T_2^{ZQ}, the zero-quantum relaxation time. The curves forming the upper and lower limits of the range correspond to T_2^{ZQ} values of 1 and 4 ms, respectively, which are ±1.5 ms of the value estimated from the reciprocal sum of the line widths (60 Hz for C′ and 73 Hz for Cα). The simulations for a parallel, in-register strand alignment overlap with the experimental Zeeman exchange data, but the simulations for an out-of-register alignment do not. The large range covered by both sets of curves nevertheless illustrates the uncertainties inherent in RR distance measurements from small $^{13}C-^{13}C$ couplings, owing to the dominant influence of T_2^{ZQ}, and so we cannot exclude completely the possibility of an out-of-register configuration on the basis of these data alone. Such a configuration would incur an energy penalty associated with unsaturated hydrogen bonds at the free termini, however. Moreover, structural studies using spectroscopic and diffraction techniques have highlighted the parallel, in-register arrangement as being the most common structural motif occurring in amyloid fibrils (*34*−*39*). Taking all these factors into consideration, it is reasonable to assume that $AMed_{42-49}$ adopts an in-register parallel configuration within the fibrils.

Higher Order Structural Analysis. Constraints on β-sheet packing geometry can be obtained in principle by detecting dipolar couplings between amino acid side groups that are known to be far apart within a single β-sheet but which may come into close contact when two or more sheets are stacked together with a typical repeating distance of 8−10 Å in the sheet direction. RR was again exploited to search for such constraints within fibrils of [U-^{13}C-NFGSV]$AMed_{42-49}$. It has been shown that selective distances between spin pairs can be measured from uniformly labeled solids, provided the two peaks of interest are sufficiently separated from peaks from other spins to which the observed pair may be coupled (*40, 41*). Here the aromatic carbons of F43 (Cϕ) are useful for this purpose, as their resonance frequencies are well separated from all other peaks in the spectrum (centered at ∼128.5 ppm). Coupling between Cϕ of F43 (abbreviated henceforth as Fϕ) and Cγ/Cγ′ of V46 (abbreviated henceforth as Vγ/Vγ′), which also resonate well away from other peaks (at 18.3 ppm), would provide a strong constraint on sheet packing. For in-register parallel β-strands, F43 and V46 are on opposite faces of a β-sheet layer, and Fϕ and Vγ/Vγ′ are too far apart (>9 Å) to interact with each another. Even without precise quantitative analysis of RR magnetization exchange curves, it is thus possible to confidently place upper limits on internuclear distances from which to constrain the β-sheet layers to specific packing geometries.

Spectra were obtained at the first order ($n = 1$) RR condition of 11 030 Hz with respect to Fϕ and Vγ/Vγ′ after creating an initial condition of difference polarization followed by a variable mixing period. A clear attenuation of the difference intensity is observed after a mixing period of 30 ms, indicating that the intermolecular Cα−C′ distance is close enough to permit the exchange of Zeeman order (Figure 5a). Coupling between the two residues was also evident in a two-dimensional exchange spectrum at the same spinning rate, manifest as a strong cross-peak correlating Fϕ and Vγ/Vγ′; the cross-peak is virtually absent when the MAS rate is ±150 Hz off RR (Figure 5c). The spectra are consistent

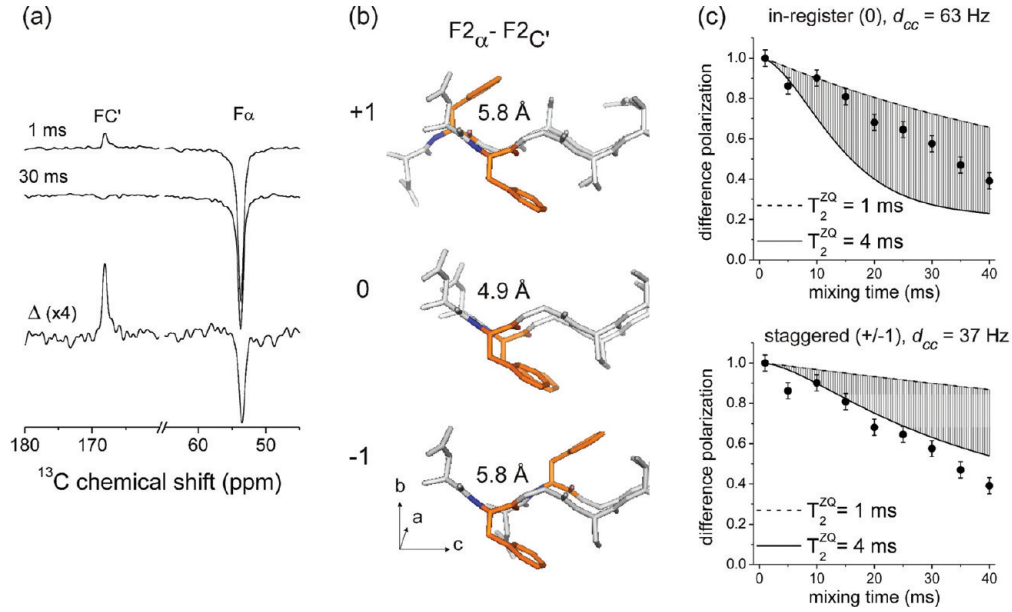

FIGURE 4: Rotational resonance ^{13}C NMR experiment to determine the alignment of hydrogen bonded β-strands in AMed$_{42-49}$ fibrils. (a) Spectra of fibrils of 5:1 [^{13}Cα-F43]AMed$_{42-49}$/[^{13}C′-F43]AMed$_{42-49}$ at $n = 1$ RR (Hz). The opposite spin polarizations created for Cα and C′ are observed after mixing times of 1 ms (top) and 30 ms (middle). A difference spectrum (bottom) obtained by subtracting the middle spectrum from the top spectrum shows the exchange of Zeeman order over 30 ms. (b) Models of hydrogen bonded strands having a parallel alignment in-register (0) or out-of-register (staggered) by +1 or −1 residue. The models are viewed along the hydrogen bonding axis and show the mean intermolecular distance between the Cα and the carbonyl carbon (C′) of F43 residues of neighboring molecules. (c) Magnetization exchange curves at $n = 1$ RR compared with numerical simulations as a function of the Cα−C′ distances for in-register (top) and staggered (bottom) strand alignments. The shaded regions are bounded by calculated curves representing the predicted upper and lower limits for each distance, reflecting uncertainties in the value of the zero-quantum relaxation time, T_2^{ZQ}. The upper and lower limits correspond to T_2^{ZQ} values of 1 and 4 ms, respectively.

with a face-to-back configuration of the sheets (i.e., classes 2 and 4 from the eight principal classes defined by Eisenberg et al. (*5*)) as this is the only arrangement that permits Fϕ and Vγ/Vγ' to come into close contact with each other for typical sheet spacings. Exchange of Zeeman order was measured at different mixing intervals between 1 and 40 ms, but the exchange curves could not be analyzed quantitatively because resonances for individual sites of the aromatic ring could not be resolved (data not presented). Instead an upper distance limit of 6.5 Å was estimated from simulations by assuming a single fictitious spin representing the centroid of the five aromatic carbons and a fictitious spin for the two valine methyl groups. These assumptions favor more rapid exchange for a given distance than is likely to occur in practice and so provides a generous estimate of the maximum distance.

Further RR measurements were able to detect coupling between Cβ of S45 (i.e., Sβ) and Vγ/Vγ' (Figure 5), which provided a second possible constraint on the sheet packing geometry. At RR with respect to these two ^{13}C spins (i.e., 4450 Hz), coupling was again manifest as the attenuation of peak intensities in the one-dimensional experiment (Figure 5b) and as cross-peaks in the two-dimensional exchange experiment (Figure 5d). In this case off-RR coupling between Vγ/Vγ' and Vα was also detected, which prevented the magnetization exchange between Sβ and Vγ/Vγ' from being analyzed quantitatively to extract a precise internuclear distance. This is because, in the presence of coupling between Vγ/Vγ' and Vα, the exchange of Zeeman order between Sβ and Vγ/Vγ' will be less rapid than for an isolated spin pair (*40, 41*) and, if the additional off-RR coupling is neglected, the measured distance will be an overestimate of the true value. By assuming the isolated two-spin approximation, the upper limit on the Sβ−Vγ/Vγ' distance was estimated to be 5.5 Å (data not presented). For this pair of sites, an additional complication is that the *intramolecular* Sβ−Vγ/Vγ' distance could be less than 6 Å for certain V46 side-chain conformations (defined by the N−Cα−Cβ−Cγ torsional angle χ_1). We therefore determined the side-chain conformation of V45 within the [U-^{13}C-NFGSV]AMed$_{42-49}$ fibrils using a two-dimensional DQ-HLF experiment to measure the Hα−Cα−Cβ−Hβ torsional angle, which is equal in value to χ_1. The evolution of ^{13}C double quantum coherence for Cα and Cβ under the local fields of Hα and Hβ over one period was consistent with an angle of ±150° (Figure 6). Despite the insensitivity of the experiment to the sign of the angle, modeling the peptide as a β-strand (using the backbone angle limits in Table 3) indicates that neither V46 conformation permits Cγ or Cγ' to fall within 6 Å of S45 Cβ. At a distance of 6 Å the calculated exchange of Zeeman order is negligible even if a relatively long zero quantum relaxation time of 4 ms is assumed. In conclusion, the coupling between S45 and V46 observed in the RR experiment (Figure 5) must originate from intersheet coupling.

Proposed Models and Validation by X-ray Fiber Diffraction. The observed constraints on the intersheet Fϕ−Vγ/Vγ' and Sβ−Vγ/Vγ' distances, together with the constraints on peptide secondary structure and β-strand alignment, suggest two principal models for the cross-β spine of the fibrils (Figure 7). Both models have a face-to-back arrangement of the sheets; however, "Model 1" has an up−down arrangement of the sheets such that the N- and C-termini of each sheet run antiparallel to each other, whereas "Model 2" has an up−up arrangement with parallel N- and C-termini. The two models share the same triad of residues (F43 and S45 of one sheet and V46 of the other) forming a pivot point

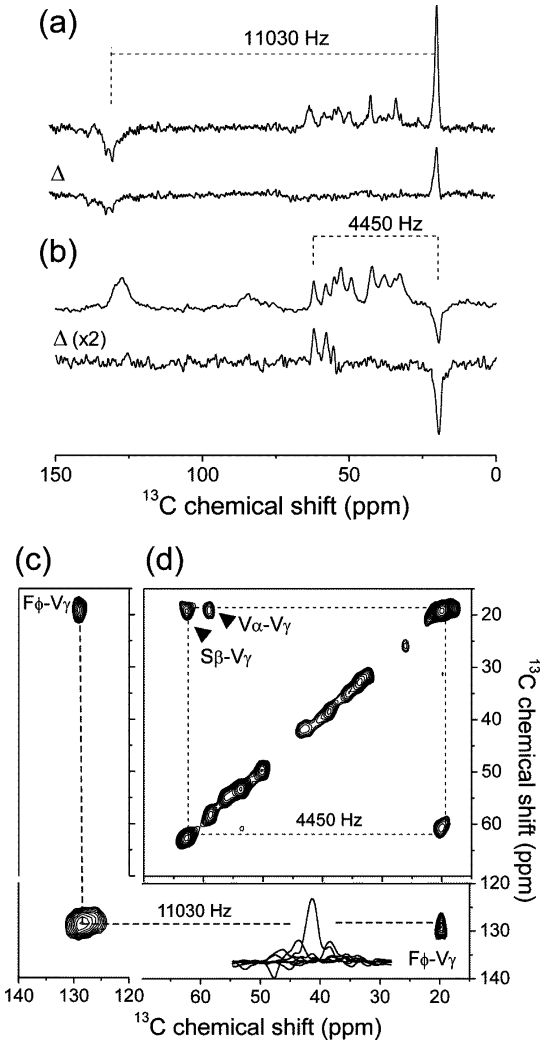

FIGURE 5: Rotational resonance ^{13}C NMR experiments to determine the packing arrangement of β-sheet layers within fibrils of [U-^{13}C,^{15}N-NFGSV]AMed$_{42-49}$. (a) One-dimensional spectra obtained by selectively inverting the spins from the F43 phenyl group (Fϕ). Spectra were obtained at a MAS rate of 11030 Hz, which is the frequency separation between the maximum of the peak envelope for Fϕ at 128.50 ppm and the superimposed peaks for Vγ/Vγ' at 18.30 ppm. The top spectrum is for a 1 ms mixing time, and the bottom spectrum is obtained by difference (exactly as described in Figure 4) showing exchange of Zeeman order over 30 ms. (b) One-dimensional spectra obtained by selectively inverting the spins for Vγ/Vγ'. Spectra were obtained at a MAS rate of 4450 Hz, which is the separation between the frequencies for Vγ/Vγ' and Sβ at 62.74 ppm. The upper and lower spectra are as described in (a). (c) A two-dimensional exchange spectrum at a MAS rate of 11030 Hz and a 30 ms mixing time, showing cross-peaks correlating Fϕ and Vγ/Vγ'. The inset shows the change in cross peak intensity as the MAS rate is swept from 10830 to 11180 Hz in 50 Hz increments. The maximum intensity occurs at 11030 Hz. (d) A two-dimensional RR spectrum at a MAS rate of 4450 Hz and 30 ms mixing time, showing cross-peaks correlating Vγ/Vγ' and Sβ (and to a lesser extent, Vα).

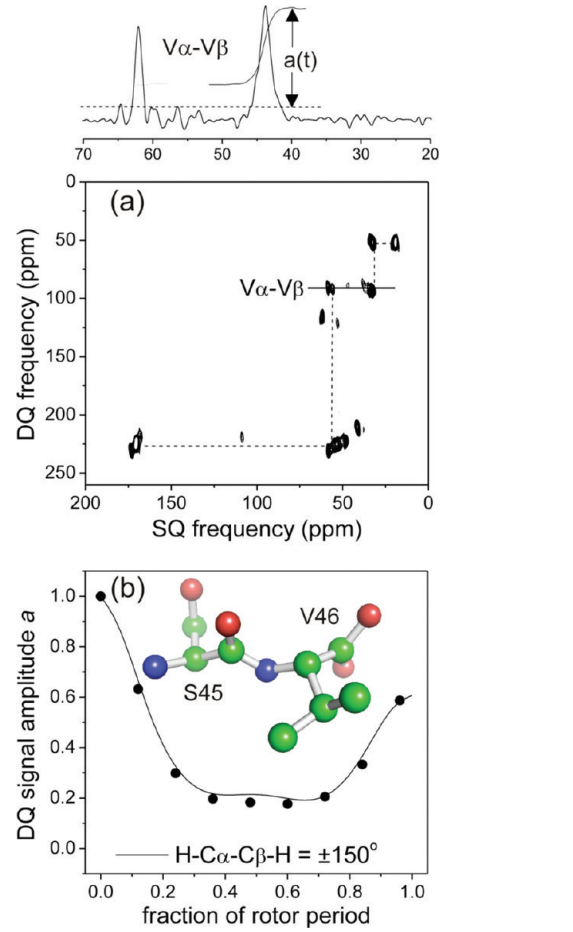

FIGURE 6: SSNMR experiment to determine side-chain Hα−Cα−Cβ−Hβ torsional angles (χ_1) for V46 in [U-^{13}C,^{15}N-NFGSV]AMed$_{42-49}$ fibrils. (a) A ^{13}C−^{13}C DQ-HLF spectrum with dotted lines showing the V46 spin system. Above the spectrum is a horizontal slice through the two-dimensional spectrum at the DQ frequency correlating Vα and Vβ. The spectrum is shown with integrals to signify that the modulated signal amplitudes $a(t)$ are calculated from the sums of the peak areas for Cα and Cβ. (b) Signal amplitudes for H−Cα−Cβ−H of V46 over one MAS cycle and a simulated curve (for $\chi_1 = 150°$) in closest agreement with the experimental data.

that dictates the relative positions of the sheets along the strand direction *c*. In a steric zipper, V46 must be intercalated between F43 and S45 to conform to both of the measured distance limits. The SSNMR measurements do not provide constraints on the spacing between the sheets, along axis *b*.

X-ray fiber diffraction from partially aligned fibrils gave a detailed, oriented diffraction pattern showing the expected features of a cross-β pattern (Figure 8). A strong meridional reflection is evident at 4.76 Å, and a strong signal is observed at 8.6 Å on the equator of the diffraction pattern. The pattern gives no indication of a layerline at 9.5 Å and therefore supports the view that the structure is composed of parallel β-sheets. Additional diffraction signals are also observed on the equator (see Figure 8 and Table 4). The two models arising from SSNMR analysis were examined with reference to the diffraction pattern. The diffraction peaks on the equator of the pattern were indexed to a possible unit cell of 29.2 Å (chain) × 36.6 Å (sheet) × 4.76 Å (H-bonding). The unit cell dimension of 36.6 Å helps to give support to Model 1, in which the pairs of sheets in an up−down arrangement relative to one another, since it would be expected that Model 2 would have a unit cell dimension corresponding to a single sheet (9.15 Å). The fact that the diffraction pattern could not be indexed to a cell dimension of 18.3 Å (i.e., a pair of sheets) suggests that the repeating unit contains four β-sheet ribbons. This could arise from two pairs of sheets that are arranged face to face, or this could be the size of the protofilament. Calculation of diffraction patterns from four sheets generated from the two structural models revealed a very good match between the experimental pattern and that generated from the antiparallel sheet model. The match to

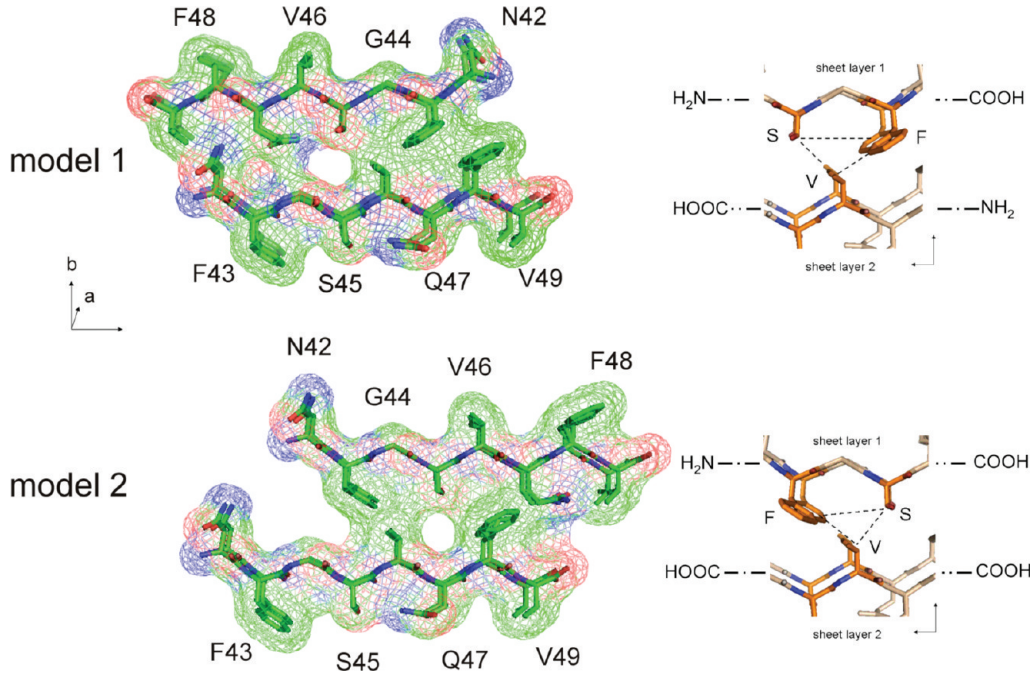

FIGURE 7: Two models of β-spine arrangements for $AMed_{42-49}$ that are consistent with the observed intersheet dipolar couplings between Fϕ and Sβ and between Vγ/Vγ' and Sβ. The models are viewed along the hydrogen bonding axis. Both models have a back-to-face stacking of the sheets, as defined by Eisenberg et al. In Model 1, two β-sheet layers have an up−down arrangement with the N- and C-termini at opposite ends. In Model 2, the sheets have an up−up arrangement with the N- and C-termini at the same ends. The β-strands have an in-register parallel alignment within each sheet.

the parallel sheet model was also reasonable, but several reflections observed in the experimental pattern were absent or very weak in the calculated pattern. This analysis gives support to the antiparallel sheet model, when the structure is composed of four sheets.

DISCUSSION

Detailed structural investigations of peptides and proteins in amyloid or amyloid-like fibrils are beginning to identify some of the common molecular features that are prevalent within protofibril elements. Studies of short model peptides have revealed a steric zipper motif for the cross-β spine conforming to eight generic structural classes (*5*). Strands may be parallel or antiparallel within β-sheets; each β-sheet may be parallel or antiparallel with respect to the other, and two sheet layers can have up−down or up−up orientations. Fibrils of different short peptide segments derived from the same parent protein often show distinct morphological differences, however, which illustrate the strong determinants of fibril substructure that are inherent in the polypeptide sequence. Such observations serve to emphasize that due caution must be taken when drawing conclusions about the fibril architecture of the parent polypeptides from which the model fragments are derived. Studies of short model peptides are nevertheless valuable for gaining insight into the variety of molecular interactions and quaternary contacts that stabilize fibrillar assemblies in general.

Here, SSNMR measurements combined with X-ray fiber diffraction provide strong constraints on the geometry of $AMed_{42-49}$ fibrils. Distance measurements using RR played a useful role in the structural analysis. The RR phenomenon has been exploited widely for structural investigations of solids containing pairs of ^{13}C labels, because by simply adjusting the sample spinning rate it is possible to selectively reintroduce and measure distance-dependent dipolar interactions between pairs of spins incorporated into organic solids. Recently the capability of RR was extended to determine distances between pairs of ^{13}C nuclei in uniformly ^{13}C-labeled solids (*41*), which were exploited to solve the molecular conformation of acetylcholine when bound to its receptor (*40*). Here, by exploiting RR measurements in one- and two-dimensions on extensively ^{13}C-labeled peptides, we suggest plausible models for the β-spine of the peptide H_2N-NFGSVQFV-COOH from the aortic amyloid medin, to add to the growing library of amyloid structural models determined by diffraction and NMR techniques.

Earlier investigations of the aggregation and fibril morphology of $AMed_{42-49}$ highlighted its amyloidogenic properties and suggested that residues 42−49 of the 50-amino acid parent protein constitute a fibrillogenic element (*17*). Here, structural constraints by SSNMR favor two models of the β-spine arrangement of $AMed_{42-29}$, both with sheet layers having a face-to-back configuration (Figure 7). The fiber diffraction pattern for the fibrils is consistent with both models if four sheets occupy the unit cell, but comparing the experimental data with calculated diffraction patterns, Model 1 is supported more strongly than Model 2. Intuitively, Model 1, in which pairs of layers are aligned antiparallel to each other, appears to be the more stable β-spine configuration because it exhibits structural elements in common with other amyloid structures. These features are absent in the parallel sheet arrangement of Model 2. In Model 1 the side groups of N42 and Q47 of opposing sheets are placed close together, allowing an extended hydrogen bonding network between the side-chain amide groups running approximately parallel with the fibril axis. Similar networks of hydrogen-bonded glutamine repeats in poly(L-glutamine) peptide fibrils give rise to polar zippers that hold together β-sheet layers

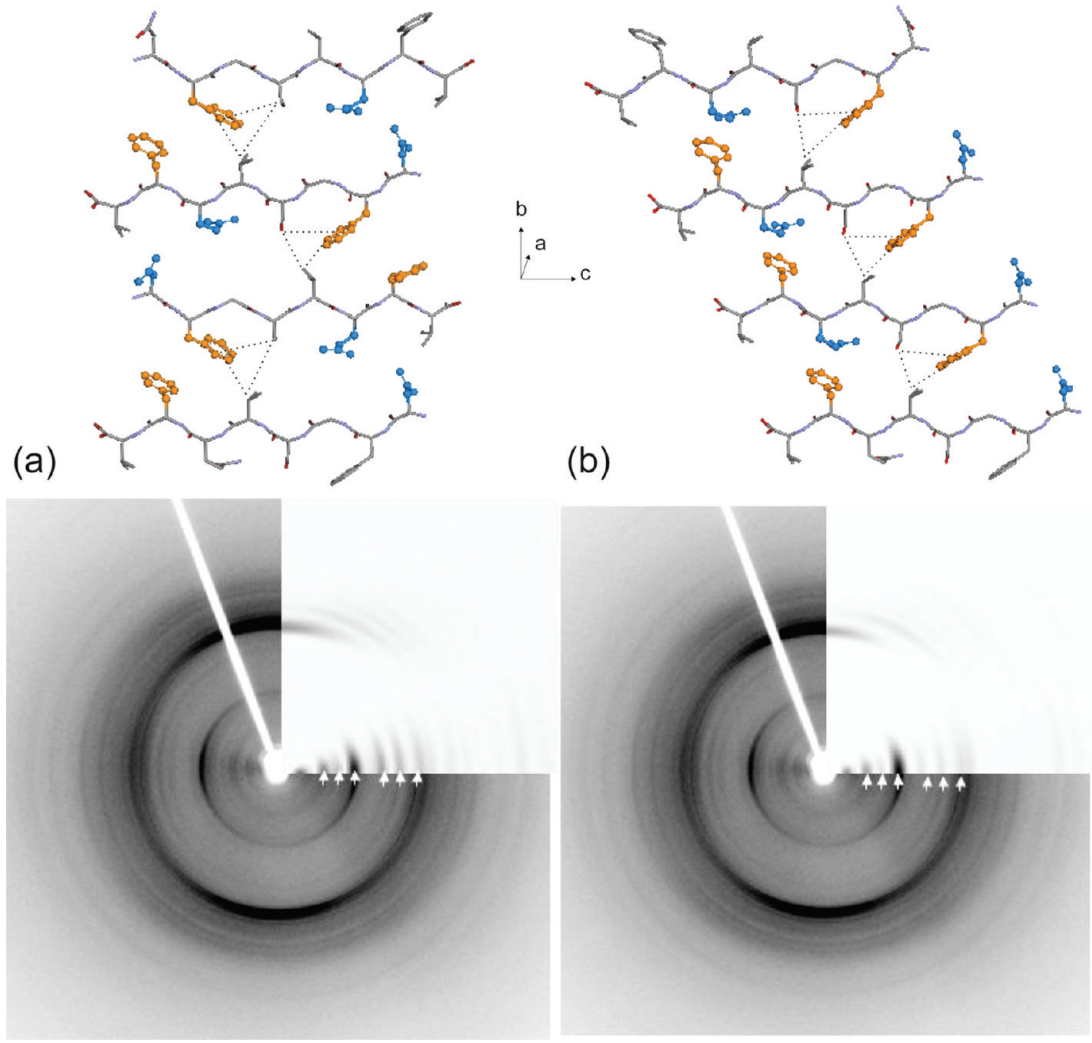

FIGURE 8: Comparison of the experimental X-ray fiber diffraction pattern for $AMed_{42-49}$ fibrils with insets showing diffraction patterns calculated from Model 1 (a) and Model 2 (b). The arrows show the key reflections. Both calculated patterns show good matches of major reflections. However, the pattern from Model 2 does not show reflections in positions where they are observed in the experimental pattern. Above each pattern are corresponding unit cell arrangements for each model (viewed along the fibril hydrogen bonding axis *a*), with four β-sheets in each cell. F43 and F48 are highlighted in orange, and N42 and Q47 are highlighted in blue. The dotted line shows the position of the F43, S45, V46 triad constrained by the NMR measurements.

Table 4: Measured Positions of Equatorial Reflections from the Experimental Diffraction Pattern Given by $AMed_{42-49}$ Fibrils with the Calculated Positions and Indexing from the Determined Unit Cell ($a = 4.76$ Å, $b = 36.6$ Å, $c = 29.2$ Å, $\alpha = \beta = \gamma = 90°$), Where *a* Is Parallel to the Fiber Axis Hydrogen Bonding Direction

observed diffraction signal position (Å)	calculated diffraction signal position (Å)	*h*	*k*	*l*
~30	29.2	1	0	0
21 (vw)	22.8	1	1	0
14.6	14.59	2	0	0
11.4	11.41	2	2	0
9.4	9.40	3	1	0
8.6	8.58	3	2	0
6.1	6.1	0	6	0

(*42*). In addition, the aromatic rings of F43 and F48 of facing sheets are situated close enough to each other to give rise to some form of stabilizing interaction. Aromatic π-stacking has been suggested to be an important stabilizing factor of amyloid in general (*21*), and experimental and in silico studies have suggested that such interactions could stabilize fibrils or oligomeric intermediates from several peptides (*43*−*45*). In the specific case of $AMed_{42-49}$, experimental studies of amino acid substituted peptides (*20*) and molecular dynamic simulations of aggregation (*46*) have both drawn attention to phenylalanine residues as being important for fibril assembly. Others have argued that aromatic $\pi-\pi$ interactions may not be important for amyloid formation and that the hydrophobicity and amyloidogenic potential of aromatic residues are more relevant factors (*47, 48*). In full length medin, replacement of F43 and F48 with alanine does not prevent amyloid formation (*19*), indicating that aromatic interactions at these positions are not exclusively responsible for self-assembly. This suggests that other sequential elements outside of the eight C-terminal residues very likely influence the aggregation potential of the full-length polypeptide. The current data do not confirm whether the intermolecular F43−F48 distance is close enough to permit overlap of their π orbitals. SSNMR experiments to detect dipolar interactions between ^{13}C-labeled Phe rings at one position and ^{2}H- or ^{19}F-labeled Phe rings at the other (*49*) would provide evidence with which to argue for or against the presence of $\pi-\pi$ interactions. Such experiments are now in progress to evaluate the structural role of aromatic interactions in $AMed_{42-49}$ and in peptides of the general sequence $NF(X)_nNF$.

Crystallographic studies of model peptides by the Eisenberg group have identified a specific steric zipper motif with "dry" interfaces characterized by short spacings between sheet layers and "wet" interfaces defined by longer sheet spacings (*4*). Here the constraints obtained by SSNMR and X-ray fiber diffraction are insufficient to determine precisely the spacing between sheets, but some conclusions can be drawn from the data. In Model 1 the sheets adopt a face-to-back arrangement of the β-sheet laminae, which implies that the sheet spacing is uniform, whereas for a face-to-face structure the sheets are more likely to alternate between wet and dry interfaces. Moreover, two or more different quaternary contacts, as in wet and dry interfaces, can give rise to peak splitting (*50*); however, here the line widths are rather narrow, and no evidence of peak doubling is observed. The rather large unit cell accommodates four β-sheet layers within a repeating distance of 36.6 Å along the sheet direction, indicating that the protofilaments consist of at least this many layers. The fibril diameter is approximately 10−20 nm (Figure 2), which suggests that several protofilaments are combined laterally or that a single protofilament consists of several unit cells. It is noted that the structural model here pertains to fibrils grown with agitation, and it is possible that fibrils adopt alternative structures when grown under quiescent conditions, for example, as reported for Aβ_{1-40} by Tycko and colleagues (*10*). The relationship between medin fibril structure and growth conditions, including temperature and pH, is currently under investigation.

The fibrillogenic properties of residues 42−29 of medin could be targeted by compounds, including peptides, that interfere with the aggregation of the full-length protein by interacting with the growing face of the fibrils and blocking further aggregation (*51*). Our recent work with the 140 amino acid protein α-synuclein associated with Lewy body diseases has demonstrated that amyloidogenic peptide fragments can be modified to create effective aggregation inhibitors when guided by structural information from SSNMR (*52*). Work is now underway to design medin inhibitors based on the sequence and β-spine structure of AMed$_{42-49}$, for use as tools to validate the pathological significance of AMA and, ultimately, for potential therapeutic purposes.

REFERENCES

1. Chiti, F., and Dobson, C. M. (2006) Protein misfolding, functional amyloid, and human disease. *Annu. Rev. Biochem. 75*, 333–366.
2. Merlini, G., and Westermark, P. (2004) The systemic amyloidoses: clearer understanding of the molecular mechanisms offers hope for more effective therapies. *J. Intern. Med. 255*, 159–178.
3. Kodali, R., and Wetzel, R. (2007) Polymorphism in the intermediates and products of amyloid assembly. *Curr. Opin. Struct. Biol. 17*, 48–57.
4. Nelson, R., Sawaya, M. R., Balbirnie, M., Madsen, A. O., Riekel, C., Grothe, R., and Eisenberg, D. (2005) Structure of the cross-beta spine of amyloid-like fibrils. *Nature 435*, 773–778.
5. Sawaya, M. R., Sambashivan, S., Nelson, R., Ivanova, M. I., Sievers, S. A., Apostol, M. I., Thompson, M. J., Balbirnie, M., Wiltzius, J. J. W., McFarlane, H. T., Madsen, A. O., Riekel, C., and Eisenberg, D. (2007) Atomic structures of amyloid cross-beta spines reveal varied steric zippers. *Nature 447*, 453–457.
6. Wiltzius, J. J. W., Sievers, S. A., Saway, M. R., Cascio, D., Popov, D., Riekel, C., and Eisenberg, D. (2008) Atomic structure of the cross-beta spine of islet amyloid polypeptide (amylin), *Protein Sci. 17*, 1467–1474.
7. Tenidis, K., Waldner, M., Bernhagen, J., Fischle, W., Bergmann, M., Weber, M., Merkle, M. L., Voelter, W., Brunner, H., and Kapurniotu, A. (2000) Identification of a penta- and hexapeptide of islet amyloid polypeptide (IAPP) with amyloidogenic and cytotoxic properties. *J. Mol. Biol. 295*, 1055–1071.
8. Heise, H. (2008) Solid-state NMR spectroscopy of amyloid proteins. *ChemBioChem 9*, 179–189.
9. Petkova, A. T., Ishii, Y., Balbach, J. J., Antzutkin, O. N., Leapman, R. D., Delaglio, F., and Tycko, R. (2002) A structural model for Alzheimer's beta-amyloid fibrils based on experimental constraints from solid state NMR. *Proc. Natl. Acad. Sci. U.S.A. 99*, 16742–16747.
10. Petkova, A. T., Leapman, R. D., Guo, Z. H., Yau, W. M., Mattson, M. P., and Tycko, R. (2005) Self-propagating, molecular-level polymorphism in Alzheimer's beta-amyloid fibrils. *Science 307*, 262–265.
11. Luca, S., Yau, W.-M., Leapman, R. D., and Tycko, R. (2007) Peptide Conformation and Supramolecular Organization in Amylin Fibrils: Constraints from Solid-State NMR. *Biochemistry 46*, 13505–13522.
12. Iwata, K., Fujiwara, T., Matsuki, Y., Akutsu, H., Takahashi, S., Naiki, H., and Goto, Y. (2006) 3D structure of amyloid protofilaments of beta(2)-microglobulin fragment probed by solid-state NMR. *Proc. Natl. Acad. Sci. U.S.A. 103*, 18119–18124.
13. Jaroniec, C. P., MacPhee, C. E., Astrof, N. S., Dobson, C. M., and Griffin, R. G. (2002) Molecular conformation of a peptide fragment of transthyretin in an amyloid fibril. *Proc. Natl. Acad. Sci. U.S.A. 99*, 16748–16753.
14. Wasmer, C., Lange, A., van Melckebeke, H., Siemer, A. B., Riek, R., and Meier, B. H. (2008) Amyloid Fibrils of the HET-s(218−289) Prion Form a β Solenoid with a Triangular Hydrophobic Core. *Science 319*, 1521–1523.
15. Heise, H., Hoyer, W., Becker, S., Andronesi, O. C., Riedel, D., and Baldus, M. (2005) Molecular-level secondary structure, polymorphism, and dynamics of full-length alpha-synuclein fibrils studied by solid-state NMR. *Proc. Natl. Acad. Sci. U.S.A. 102*, 15871–15876.
16. Peng, S. W., Westermark, G. T., Sletten, K., Glennert, J., and Westermark, P. (2001) Distribution of medin-amyloid in aging and in association with arterial diseases. *Amyloid 8*, 122–123.
17. Haggqvist, B., Naslund, J., Sletten, K., Westermark, G. T., Mucchiano, G., Tjernberg, L. O., Nordstedt, C., Engstrom, U., and Westermark, P. (1999) Medin: An integral fragment of aortic smooth muscle cell-produced lactadherin forms the most common human amyloid. *Proc. Natl. Acad. Sci. U.S.A. 96*, 8669–8674.
18. Peng, S., Larsson, A., Wassberg, E., Gerwins, P., Thelin, S., Fu, X., and Westermark, P. (2007) Role of aggregated medin in the pathogenesis of thoracic aortic aneurysm and dissection. *Lab. Invest. 87*, 1195–1205.
19. Larsson, A., Soderberg, L., Westermark, G. T., Sletten, K., Engstrom, U., Tjernberg, L. O., Naslund, J., and Westermark, P. (2007) Unwinding fibril formation of medin, the peptide of the most common form of human amyloid. *Biochem. Biophys. Res. Commun. 361*, 822–828.
20. Reches, M., and Gazit, E. (2004) Amyloidogenic hexapeptide fragment of medin: homology to functional islet amyloid polypeptide fragments. *Amyloid 11*, 81–89.
21. Gazit, E. (2002) A possible role for pi-stacking in the self-assembly of amyloid fibrils. *FASEB J. 16*, 77–83.
22. Bennett, A. E., Rienstra, C. M., Auger, M., Lakshmi, K. V., and Griffin, R. G. (1995) *J. Chem. Phys. 103*, 6951.
23. Takegoshi, K., Nakamura, S., and Terao, T. (2001) C-13-H-1 dipolar-assisted rotational resonance in magic-angle spinning NMR. *Chem. Phys. Lett. 344*, 631–637.
24. Feng, X., Lee, Y. K., Sandstrom, D., Eden, M., Maisel, H., Sebald, A., and Levitt, M. H. (1996) Direct determination of a molecular torsional angle by solid-state NMR. *Chem. Phys. Lett. 257*, 314–320.
25. Lee, Y. K., Kurur, N. D., Helmle, M., Johannessen, O. G., Nielsen, N. C., and Levitt, M. H. (1995) Efficient Dipolar Recoupling in the NMR of Rotating Solids - a Sevenfold Symmetrical Radiofrequency Pulse Sequence. *Chem. Phys. Lett. 242*, 304–309.
26. Lee, M., and Goldburg, W. I. (1965) Nuclear-Magnetic-Resonance Line Narrowing by a Rotating Rf Field. *Phys. Rev. A 140*, 1261–1271.
27. Levitt, M. H., Raleigh, D. P., Creuzet, F., and Griffin, R. G. (1990) Theory and Simulations of Homonuclear Spin Pair Systems in Rotating Solids. *J. Chem. Phys. 92*, 6347–6364.
28. Makin, O. S., and Serpell, L. C. (2005) In *Amyloid proteins: methods and protocols* (Sigurdsson, E. M., Ed.), pp 67−80, Humana press, Totowa, NJ.

29. Makin, O. S., Sikorski, P., and Serpell, L. C. (2007) CLEARER: a new tool for the analysis of X-ray fibre diffraction patterns and diffraction simulation from atomic structural models. *J. Appl. Crystallogr. 40*, 966–972.
30. Cornilescu, G., Delaglio, F., and Bax, A. (1999) Protein backbone angle restraints from searching a database for chemical shift and sequence homology. *J. Biomol. NMR 13*, 289–302.
31. Thompson, L. K., McDermott, A. E., Raap, J., Vanderwielen, C. M., Lugtenburg, J., Herzfeld, J., and Griffin, R. G. (1992) Rotational Resonance Nmr-Study of the Active-Site Structure in Bacteriorhodopsin - Conformation of the Schiff-Base Linkage. *Biochemistry 31*, 7931–7938.
32. Raleigh, D. P., Levitt, M. H., and Griffin, R. G. (1988) Rotational Resonance in Solid-State Nmr. *Chem. Phys. Lett. 146*, 71–76.
33. Madine, J., Jack, E., Stockley, P. G., Radford, S. E., Serpell, L. C., and Middleton, D. A. (2008) Structural insights into the polymorphism of amyloid-like fibrils formed by region 20−29 of amylin revealed by solid-state NMR and X-ray fibre diffraction. *J. Am. Chem. Soc. 130*, 14990–15001.
34. Cobb, N. J., Sonnichsen, F. D., McHaourab, H., and Surewicz, W. K. (2007) Molecular architecture of human prion protein amyloid: A parallel, in-register beta-structure. *Proc. Natl. Acad. Sci. U.S.A. 104*, 18946–18951.
35. Zheng, J., Jang, H., Ma, B., Tsai, C. J., and Nussinov, R. (2007) Modeling the Alzheimer A beta(17−42) fibril architecture: Tight intermolecular sheet-sheet association and intramolecular hydrated cavities. *Biophys. J. 93*, 3046–3057.
36. Chen, M., Margittai, M., Chen, J., and Langen, R. (2007) Investigation of alpha-synuclein fibril structure by site-directed spin labeling. *J. Biol. Chem. 282*, 24970–24979.
37. Margittai, M., and Langen, R. (2008) Fibrils with parallel in-register structure constitute a major class of amyloid fibrils: molecular insights from electron paramagnetic resonance spectroscopy. *Q. Rev. Biophys. 41*, 265–297.
38. Paravastua, A. K., Leapman, R. D., Yau, W. M., and Tycko, R. (2008) Molecular structural basis for polymorphism in Alzheimer's beta-amyloid fibrils. *Proc. Natl. Acad. Sci. U.S.A. 105*, 18349–18354.
39. Kim, Y. S., Liu, L., Axelsen, P. H., and Hochstrasser, R. M. (2008) Two-dimensional infrared spectra of isotopically diluted amyloid fibrils from A beta 40. *Proc. Natl. Acad. Sci. U.S.A. 105*, 7720–7725.
40. Williamson, P. T. F., Verhoeven, A., Miller, K. W., Meier, B. H., and Watts, A. (2007) The conformation of acetylcholine at its target site in the membrane-embedded nicotinic acetylcholine receptor. *Proc. Natl. Acad. Sci. U.S.A. 104*, 18031–18036.
41. Verhoeven, A., Williamson, P. T. F., Zimmermann, H., Ernst, M., and Meier, B. H. (2004) Rotational-resonance distance measurements in multi-spin systems. *J. Magn. Reson. 168*, 314–326.
42. Perutz, M. F., Johnson, T., Suzuki, M., and Finch, J. T. (1994) Glutamine Repeats as Polar Zippers - Their Possible Role in Inherited Neurodegenerative Diseases. *Proc. Natl. Acad. Sci. U.S.A. 91*, 5355–5358.
43. Mazor, Y., Gilead, S., Benhar, I., and Gazit, E. (2002) Identification and characterization of a novel molecular-recognition and self-assembly domain within the islet amyloid polypeptide. *J. Mol. Biol. 322*, 1013–1024.
44. Zhang, Z. Q., Chen, H., Bai, H. J., and Lai, L. H. (2007) Molecular dynamics Simulations on the oligomer-formation process of the GNNQQNY peptide from yeast prion protein sup35. *Biophys. J. 93*, 1484–1492.
45. Makin, O. S., Atkins, E., Sikorski, P., Johansson, J., and Serpell, L. C. (2005) Molecular basis for amyloid fibril formation and stability. *Proc. Natl. Acad. Sci. U.S.A. 102*, 315–320.
46. Gazit, E., della Bruna, P., Pieraccini, S., and Colombo, G. (2007) The molecular dynamics of assembly of the ubiquitous aortic medial amyloidal medin fragment. *J. Mol. Graphics 25*, 903–911.
47. Bemporad, F., Taddei, N., Stefani, M., and Chiti, F. (2006) Assessing the role of aromatic residues in the amyloid aggregation of human muscle acylphosphatase. *Protein Sci. 15*, 862–870.
48. Marek, P., Abedini, A., Song, B. B., Kanungo, M., Johnson, M. E., Gupta, R., Zaman, W., Wong, S. S., and Raleigh, D. P. (2007) Aromatic interactions are not required for amyloid fibril formation by islet amyloid polypeptide but do influence the rate of fibril formation and fibril morphology. *Biochemistry 46*, 3255–3261.
49. Jack, E., Newsome, M., Stockley, P. G., Radford, S. E., and Middleton, D. A. (2006) The organization of aromatic side groups in an amyloid fibril probed by solid-state H-2 and F-19 NMR spectroscopy. *J. Am. Chem. Soc. 128*, 8098–8099.
50. Lee, S. W., Mou, Y., Lin, S. Y., Chou, F. C., Tseng, W. H., Chen, C., Lu, C. Y. D., Yu, S. S. F., and Chan, J. C. C. (2008) Steric zipper of the amyloid fibrils formed by residues 109−122 of the Syrian hamster prion protein. *J. Mol. Biol. 378*, 1142–1154.
51. Sciarretta, K. L., Gordon, D. J., Meredith, S. C. (2006) Peptide-based inhibitors of amyloid assembly, in *Amyloid, Prions, and Other Protein Aggregates, Part C* (Kheterpal, I., Wetzel, R., Eds.) pp 273−312, Academic Press, New York.
52. Madine, J., Doig, A. J., and Middleton, D. A. (2008) Design of an N-methylated peptide inhibitor of alpha-synuclein aggregation guided by solid-state NMR. *J. Am. Chem. Soc. 130*, 7873–7881.

BI802164E